AIAA JOURNAL
Vol. 35, No. 10, October 1997

Design Diagrams for Reliable Layered Materials

S. Mark Spearing*
Massachusetts Institute of Technology, Cambridge, Massachusetts 02139

Many components and structures consist of two or more layers of dissimilar materials bonded together over areas that are large relative to the layer thickness. A methodology is presented that is appropriate for designing against failure due to thermomechanical loading in these systems. Results are presented for the fracture of two-layered systems of elastic materials under uniform thermal loading. In such a system of two or more materials, failure occurs as the result of four competing fracture modes. This competition is assessed, and the conditions are identified for one fracture mode to occur in preference to the others. The results are presented as fracture mechanism diagrams, which give easily interpreted guidance for the design and manufacture of layered materials. The same graphical format can be used to map performance metrics relevant to functional requirements other than reliability, such as heat flow, curvature, and mass per unit area. These diagrams are potentially useful for the preliminary design of components with multiple performance requirements.

I. Introduction

A DIVERSE range of aerospace components and structures can be modeled as continuously bonded layers of dissimilar materials. Examples include many electronic packages,[1,2] thermal barrier coatings,[3] active structures,[4] and adhesive lap joints.[5] In each of these examples, the component has multiple functional requirements that must be satisfied, involving aspects of mechanical, thermal, electrical, and chemical performance. In many of these applications, thermomechanical reliability is also a major concern, by virtue of the stresses that arise when dissimilar materials are bonded and the temperature is varied.[6] Under these conditions, failure may occur by the fracture of one or another of the layers or the interface between them. Notwithstanding the importance of reliability, it is rarely included in the preliminary design process on an equal basis with the other functional requirements. The purpose of this paper is to outline a simple engineering approach to the design of such components. The key is to adopt a methodology whereby all of the functional requirements, including reliability, can be assessed simultaneously. To achieve this goal, it is necessary to adopt a sufficiently simple model for the component geometries, while retaining the features that govern performance.

The simplest relevant problem is to consider the design of components consisting of only two layers, which deform in a linear elastic–brittle manner. Simplifying the problem to this degree allows the results to be presented in a readily interpreted graphical format. The assumption of brittle–elastic behavior gives conservative lower bounds for failure. In practice, plasticity, viscoelasticity, or creep may serve to limit the stress levels induced in the materials. The restriction of the analysis to two layers is for the purpose of illustration only. The same analytical approach can be applied equally well to components consisting of three or more layers.

The structure of the paper is as follows. In Sec. II, the failure modes and necessary mechanics of an elastic bimaterial strip under uniform thermal loading are reviewed. In Sec. III, these analyses are combined with the appropriate failure criteria for brittle–elastic materials to construct failure mode mechanism diagrams. In Sec. IV, simple models for other performance metrics are represented on the same diagrams to create multifunctional design diagrams for three example components. These diagrams are a useful aid in the course of the preliminary design of layered components and can also serve as an educational tool.

II. Mechanics of a Bimaterial Strip

Experimental observations of bimaterial bilayers under thermal loading show that there are four possible failure modes: crazing of one or the other layer, interfacial fracture, and spalling.[6–9] These are shown schematically in Fig. 1. To understand the conditions to initiate each of these failure modes and the competition between them, it is necessary to understand the stress state that results from the purely thermal loading of a bimaterial strip.

The bimaterial strip has been of long standing interest to engineers, due to its convenience as a temperature measuring device. The stress and strain distributions under the application of a uniform change in temperature, consequently, are well understood and can be analyzed using simple beam theory, together with assumptions of equilibrium and compatibility of curvatures and the interfacial strains of the two materials.[10,11]

The four nondimensional geometric and material parameters required to describe the resulting stresses, deformations, and elastic strain energy are defined as[12–14] follows.

The ratio of the layer thicknesses

$$\xi = t_1/t_2 \tag{1}$$

the elastic mismatch parameter[13]

$$A = \frac{\bar{E}_1 - \bar{E}_2}{\bar{E}_1 + \bar{E}_2} \tag{2}$$

the ratio of the elastic moduli

$$\lambda = \bar{E}_1/\bar{E}_2 \,[= (1+A)/(1-A)] \tag{3}$$

the free thermal strain

$$\varepsilon_t = (\alpha_1 - \alpha_2)\Delta T \tag{4}$$

where $t_{1,2}$ are the thicknesses of the layers, $\bar{E}_{1,2}$ are the effective Young's moduli, $\alpha_{1,2}$ are the coefficients of thermal expansion, and ΔT is the temperature change. The stress state that exists in each of the materials is equivalent to the application of a uniform in-plane force per unit width P_j and a bending moment per unit width M_j given by

$$P_1 = -\xi\beta t_1(\lambda\xi^3 + 1) \tag{5a}$$

$$P_2 = +\xi\beta t_1(\lambda\xi^3 + 1) \tag{5b}$$

$$M_1 = +\tfrac{1}{2}\lambda\xi^3\beta t_1^2(\xi + 1) \tag{5c}$$

$$M_2 = +\tfrac{1}{2}\beta t_1^2(\xi + 1) \tag{5d}$$

where

$$\beta = \frac{\varepsilon_t E_1}{\xi(\lambda\xi^3 + 1)(\lambda\xi + 1) + 3\lambda\xi^2(\xi + 1)^2}$$

Temperature increases, tensile forces, and clockwise bending moments on rightward facing sections are defined as positive.

Received Jan. 24, 1997; accepted for publication June 16, 1997.

*Assistant Professor, Technology Laboratory for Advanced Composites, Department of Aeronautics and Astronautics. Member AIAA.

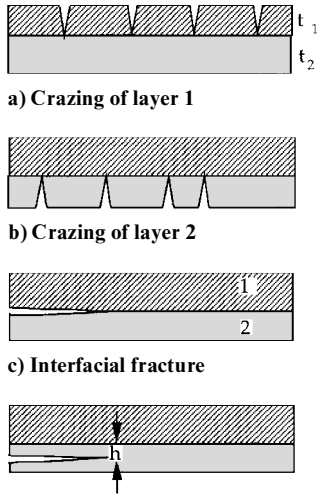

Fig. 1 Schematic representations.

A. Crazing Stresses

The onset of crazing is governed by the in-plane tensile stresses exceeding the local material strength. In each layer the stress varies linearly across the thickness, and the extreme in-plane stresses act at the interface and at the outer ligament of each layer. These stresses are designated σ_{ji} and σ_{jo} (where $j = 1$ or 2 according to the layer), respectively, and are given by beam theory as

$$\sigma_{1i} = \xi[4\lambda\xi^3 + 3\lambda\xi^2 + 1]\beta \tag{6a}$$

$$\sigma_{2o} = \xi^2[\lambda\xi^3 - 3\xi - 2]\beta \tag{6b}$$

If layer 1 is arbitrarily assumed to have the higher coefficient of thermal expansion (CTE), upon cooling P_1 is tensile and P_2 is compressive. The peak tensile stresses in each layer are then σ_{1i} and σ_{2o}, respectively; these are plotted as a function of ξ, in Figs. 2a and 2b. When one layer is thin relative to the other, the expected result for a thin film is recovered, namely, that the stress is given by the free thermal strain multiplied by the modulus of the film.[14,15] For intermediate ratios of the layer thicknesses, the bending stress varies with elastic mismatch and layer thickness, exhibiting a local maximum for a value of ξ near unity. An important observation is that σ_{2o} may be quite large and tensile, even though the mean stress is compressive. This is due to the effect of the bending moment acting on the layer.

B. Interfacial Strain Energy Release Rate

Interfacial fracture is a steady-state fracture problem in which the total stored strain energy is available to propagate the crack on the interface plane under locally mixed mode loading. The strain energy stored in a bimaterial beam, per unit length, subject to a temperature change is given by

$$\mathcal{U} = \frac{\beta^2\xi^2 t_1(\lambda\xi^3 + 1)}{2E_1}[\xi^2(\lambda\xi+1)(\lambda\xi^3+1) + 3\lambda\xi^3(\xi+1)^2] \tag{7}$$

This can be equated to the area of crack surface created as the crack is allowed to propagate by an amount δa. This is equivalent to advancing a control volume containing the crack tip by δa. This approach has been widely used for steady-state fracture problems, because it is convenient and circumvents the need for directly analyzing the crack tip stress field. The strain energy release rate is given by

$$\mathcal{G} = \mathcal{U} \tag{8}$$

This expression is plotted in Fig. 3. The thin film solution[8] of

$$\mathcal{G} = \tfrac{1}{2}E_1 t_1[(\alpha_1 - \alpha_2)\Delta T]^2 \tag{9}$$

is obtained for the case of a thin film of layer 1 on layer 2.

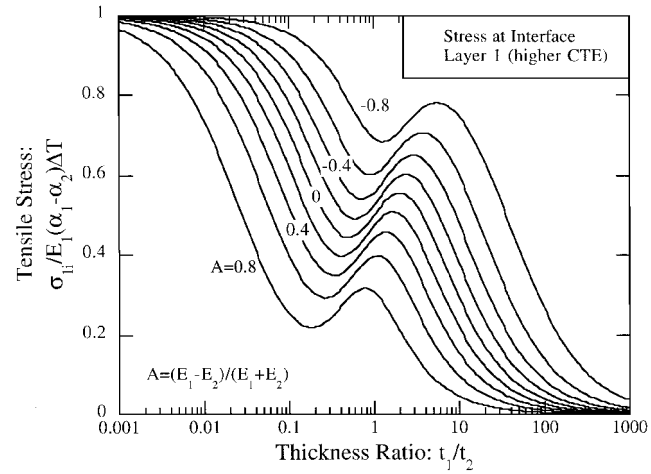

a) Material 1

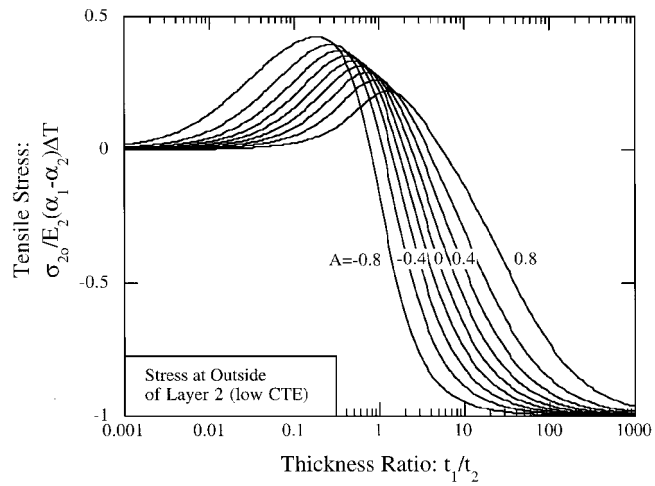

b) Material 2

Fig. 2 Maximum tensile stress.

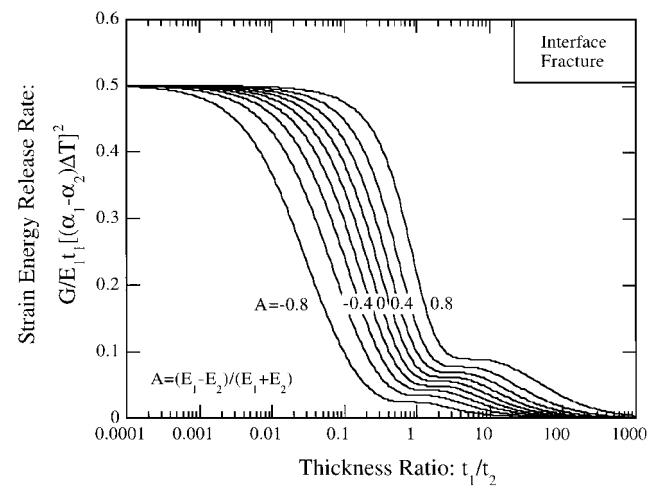

Fig. 3 Strain energy release rate vs thickness ratio for interfacial fracture.

C. Strain Energy Release Rate for Spalling

Spalling is a steady-state fracture mode, in which the crack follows a mode 1 path, parallel to but not at the interface. To evaluate the strain energy release rate for spalling, it is first necessary to calculate the standoff distance h of the crack from the interface. Suo and Hutchinson[12] have solved this problem by formulating an integral equation based on a kernel solution derived by considering an array of continuously distributed edge dislocations. Their solutions are specifically focused on the case of spallation due to a thin film

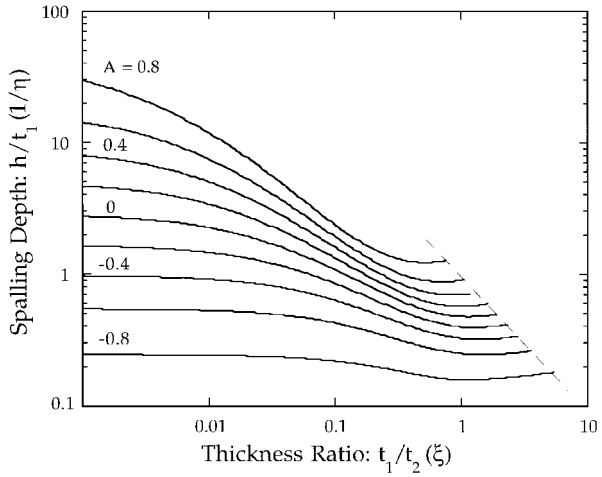

Fig. 4 Spalling depth h/t_1 vs thickness ratio ξ for a range of elastic mismatch A.

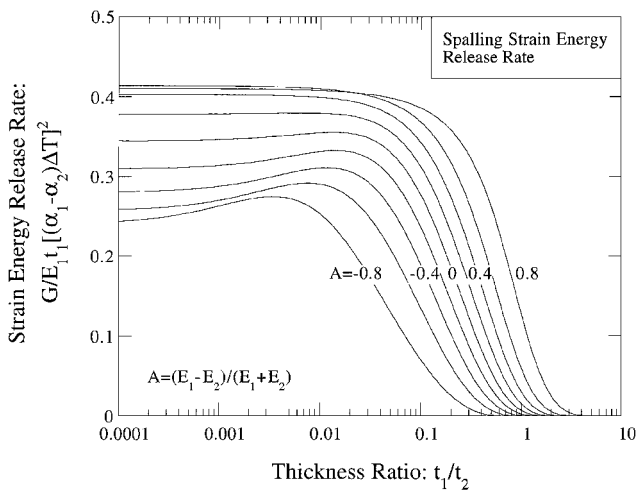

Fig. 5 Spalling strain energy G_s release rate as a function of thickness ratio ξ and A.

on a thick substrate, but they are also valid for cases where ξ approaches unity. The method is described in detail in the Appendices to their paper[12] and the expressions for the mode 1 and 2 stress intensity factors (K_1 and K_2) can be obtained directly from Eq. (11) and Appendix A of Ref. 12. The angle ω, which appears in Eq. (11) of Ref. 12, is only weakly affected by changes in the elastic mismatch; hence, it is assumed constant in this article at 52 deg, as is suggested in Ref. 12. In the present work, solutions for $K_2 = 0$ are obtained by applying a Newton–Raphson iterative routine to Suo and Hutchinson's[12] equations. The computed distance of the crack plane from the interface plane h is plotted as a function of thickness ratio ξ in Fig. 4. The crack trajectory is a strong function of both the modulus mismatch and the thickness ratio. There is a limit to the occurrence of spallation, defined by the thickness ratio for which no mode 1 path exists within layer 2. This limit varies with modulus mismatch and is shown as a dashed line in Fig. 4. This is of practical importance as it is possible to choose a value of ξ for which spalling is not a concern.

Given the distance h of the crack from the interfacial plane, it is straightforward to determine the strain energy release rate for spallation in a similar manner to that used for interfacial fracture. In contrast to interfacial fracture, not all of the elastic strain energy is available to propagate the crack. Some residual strain energy remains stored in the bimaterial in the crack wake. This is given by the same expression as in Eq. (7), with the substitution of $\eta (= t_1/h)$ for ξ,

$$\mathcal{U} = \frac{\beta^2 \eta^2 t_1 (\lambda\eta^3 + 1)}{2E_1}[\eta^2(\lambda\eta + 1)(\lambda\eta^3 + 1) + 3\lambda\eta^3(\eta + 1)^2] \tag{10}$$

The difference between this residual strain energy and the total strain energy represents the steady-state strain energy release rate for the spalling crack,

$$G_{\text{spall}} = \mathcal{U} - \mathcal{U} \tag{11}$$

This is plotted for a range of values of A against ξ in Fig. 5. The nonzero value of $\mathcal{U}$ implies that the strain energy release rate for spalling is less than that for interfacial fracture for any value of ξ. The curves intercept $G = 0$ in contrast to those for interfacial fracture, which have the thin film strain energy release rates as asymptotes for extreme values of ξ.

The solutions for strain energy release rates and stresses in the bimaterial beam can now be used to construct failure mode diagrams; this is the subject of the next section.

III. Failure Mechanism Diagrams

A. Failure Criteria

To make use of the mechanics solutions presented in Sec. II, it is necessary to equate them to appropriate failure criteria. For the case of crazing this is the strength σ_f, and for the case of spallation, it is the toughness $\mathcal{G}$ of the materials. Both the strength and toughness may be obtained by conventional mechanical test techniques. For interfacial fracture, an effective toughness may be assigned, based on tests on interfacial fracture specimens.[16–18] Ideally, specimens should be used with a similar mode mixity of loading to that present in the case of purely thermal loading.

The use of a bulk material strength may underestimate the stress to cause fracture, particularly of thin films, due to two effects. First, because thin film cracking is a tunnel cracking phenomenon, the cracking stress is governed by the toughness and film thickness.[6] Second, as with all brittle materials, the stochastic nature of the material strength leads to increasing strengths in smaller volumes of material. However, for the intended scope and application in the material selection and preliminary design phase, the use of a deterministic, thickness-independent strength is sufficient and can be chosen so as to generate conservative design choices.

B. Failure Mode Diagrams

The use of a strength of materials and steady-state fracture solutions allows the description of the conditions for failure by each of the four fracture modes solely in terms of material and interfacial properties, the absolute and relative thicknesses of the layers, and the applied temperature change. For a given pair of materials, it is possible to allow any two relevant parameters to vary while holding the others constant. In this way, two-dimensional diagrams can be constructed on which the boundaries of the individual failure modes are clearly delineated and from which the conditions for fracture can be directly assessed. There are several possible formats for such diagrams; the three most useful will be presented here. For consistency each diagram will be constructed for the case of a silicon carbide fiber (SiC_f) reinforced calcium alumino silicate (CAS) ceramic matrix composite (CMC) bonded to alumina (Al_2O_3). Table 1 shows the properties of these materials.[19,20] The failure mode diagrams are constructed for the case of cooling from an elevated stress-free temperature. Equivalent diagrams could be constructed for the case of heating, although these are of less interest and have less relevance as the stress-free temperature usually is governed by the solidification of the bonding medium.

1. *Adhesion Diagram*

The simplest diagram that can be constructed illustrates the competition between interfacial fracture and spallation. Spallation is controlled by the bulk toughness of the substrate; in contrast, local

Table 1 Properties of alumina and SiC_f/CAS CMC

	CMC	Alumina
Young's modulus E, GPa	130	370
CTE, $\alpha \times 10^{-6}$/K	4	8
Tensile strength σ_f, MPa	140	500
Toughness $\mathcal{G}$, J/m^2	25	40

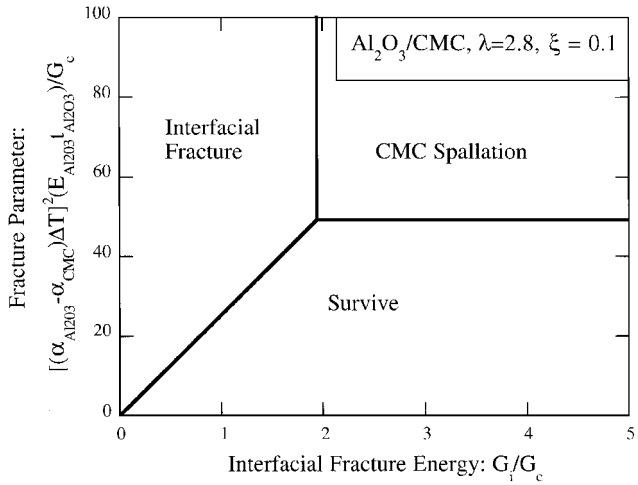

Fig. 6 Fracture diagram for adhesion as a function of interfacial fracture energy $\mathcal{G}_1/\mathcal{G}$ for an alumina–SiC/CAS CMC bilayer.

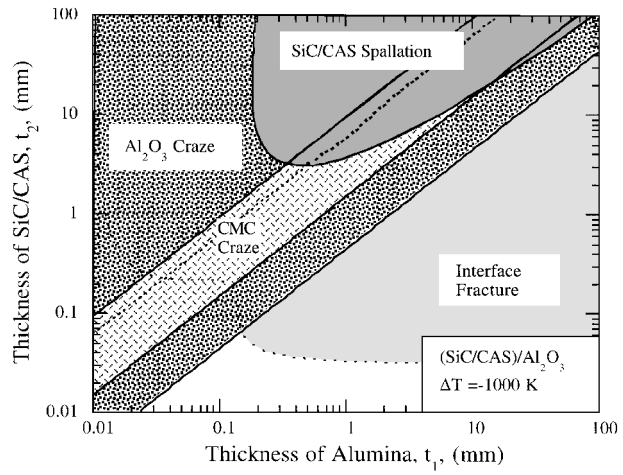

Fig. 7 Failure modes defined according to layer thickness for an alumina/CMC bilayer.

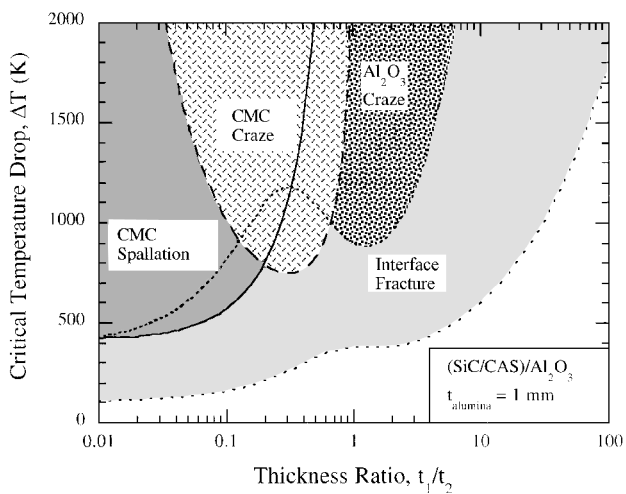

Fig. 8 Critical temperature drop diagram for alumina–SiC/CMC bilayer.

conditions at the interface govern interfacial fracture. The interfacial fracture energy may be wholly uncoupled from the properties of either or both adherends. By a suitable choice of bonding method, the interfacial toughness may be controlled, whereas the fracture properties of the bulk material are less readily tailored. The key information is, therefore, how tough the interface must be, relative to the adherends, to avoid interfacial fracture. This competition can be readily assessed for a fixed relative thickness of a given pair of materials by plotting the nondimensional critical strain energy release rate for spalling on one axis against the fracture energy of the interface relative to that of the lower CTE material. The resulting diagram is shown in Fig. 6. The ratio of the interfacial toughness to the delamination toughness of the CMC that guarantees failure by spallation rather than interfacial failure is 1.95 for this pair of materials at this thickness ratio. This reflects the higher strain energy release rate for interfacial fracture. The conditions for survival are also clearly identified in terms of the design parameters that can be selected, namely, the absolute thickness of one of the layers (ξ is already selected), the maximum allowable temperature drop (either in manufacturing or in service), and the interfacial fracture resistance. The tradeoff between these parameters can be readily explored through the graphical representation.

2. Layer Thickness Diagram

A second diagrammatic representation of the failure modes can be obtained by fixing the temperature change and the interfacial toughness and allowing the thickness of the two layers to vary. The interfacial toughness is assumed equal to that of the CMC layer, but is shown as a slightly shaded region bounded by a dashed line, indicating that the interfacial fracture energy is determined independently from either of the adherend materials. The resulting diagram is shown in Fig. 7, for a temperature drop of 1000 K. The four failure regimes are clearly visible, and the combination of layer thicknesses for which each can occur can be read directly from the diagram.

3. Critical Temperature Drop Diagram

The third failure mode diagram of interest is for the case where one layer thickness and interfacial fracture energy can be prespecified and the temperature change and thickness of the second layer are to be determined. An example of this diagram for an alumina/CMC bilayer is shown in Fig. 8. As in the preceding example, the conditions to induce each of the failure modes are clearly delineated. This format is particularly useful if it is desired to distinguish between potential bonding methods, such as diffusion bonding, brazing, and soldering, each of which has a characteristic process temperature range.

IV. Multifunctional Design Diagrams

The choice of assumptions resulting in the reduction of the conditions for fracture of bilayers to functions of the layer thickness, temperature drop, and material or interface properties and the subsequent graphical presentation of the failure modes has additional benefits. As discussed in the Introduction, in many instances components are manufactured with a layered architecture to fulfill multiple functional requirements. For cases where the layer thicknesses are small relative to the in-plane dimensions of the layers, in addition to the mechanics solutions, many of the other functional requirements can also be modeled in a way that only utilizes the layer thicknesses and material properties. So long as this is the case, performance contours can be plotted on the same axes as used for the failure mode diagrams presented in the preceding section. The two key steps are to 1) unambiguously state the functional requirements of the layered component and 2) reduce the models for the performance to a form that are either zero dimensional, one dimensional, or axisymmetric. To illustrate this concept three case studies are presented. The statements of the performance requirements are deliberately simplified to more readily illustrate the concept.

A. Metal Clad Ceramic Substrates for Power Electronics

The basic embodiment of a widely used substrate for power electronic components consists of a layer of metal conductor (often copper) directly bonded to a ceramic insulator (often alumina).[21] One or more silicon dies are bonded to the copper face, which can be etched or stamped to provide input–output connections. For the purposes of preliminary design the dies can be considered only as heat sources, and the reliability of the die itself is not considered. A schematic of the arrangement is shown in Fig. 9.

The functional requirements of the substrate can be listed as follows.

Table 2 Properties of metal/ceramic substrate constituents

	Cu	Al_2O_3	AlN
Young's modulus E, GPa	125	370	325
CTE, $\alpha \times 10^{-6}$/K	17	8	4
Tensile strength σ_t, MPa	——	500	400
Toughness G_c, J/m^2	——	40	40
Conductivity κ, W/mK	398	21	200

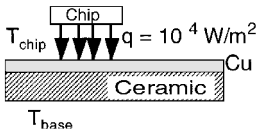

Fig. 9 Schematic of a metal/ceramic laminated substrate used for power electronics.

1) The copper must carry high currents without causing excessive ohmic heating. This defines a minimum thickness of the copper, e.g., 0.125 mm.

2) The ceramic provides electrical insulation. A minimum thickness of 0.65 mm is required such that voltage breakdown does not occur between the copper and the baseplate to which the substrate would be attached.

3) The substrate must conduct heat away from the chip, so that the surface temperature of the chip remains below a given temperature. For illustrative purposes, it is assumed here that the chip generates a heat flux q of 10^4 W/m^2, that the surface temperature T_{chip} of the copper must be kept below 373 K, and that the temperature of the outer face of the ceramic T_{base} can be maintained at 298 K. By one-dimensional heat flow, these quantities are related by

$$T_{chip} = T_{base} + q[(t_1/\kappa_1) + (t_2/\kappa_2)] \tag{12}$$

where κ_1 and κ_2 are the thermal conductivities of the two layers.

4) The device must survive thermal cycling of (223 K/423 K), which defines a temperature change ΔT of 200 K.

At the preliminary stage, the designer might be interested in whether the alumina substrate can be replaced by aluminum nitride, a high thermal conductivity ceramic. The relevant properties of the constituent materials are shown in Table 2. These properties are used to construct the design diagrams shown in Figs. 10a and 10b.

The functional requirements 1 and 2 are essentially fixed for this example and define minimum gauge thicknesses for the copper and ceramic. For copper on alumina, the diagram shows that the design is most severely constrained by the requirement of maintaining the chip temperature below 373 K, due to the relatively low thermal conductivity of the ceramic.

For the case of aluminum nitride, the much higher thermal conductivity significantly reduces the constraint imposed by maintaining a low chip temperature. However, the greater disparity in thermal expansion coefficients between AlN and Cu means that the design is severely constrained by the possibility of ceramic spallation. For both designs, the allowable design space is uncomfortably small. A designer confronted with this choice would be well advised to return to the functional requirements and reevaluate whether there is any scope for relaxation in the functional requirements. If the thermal cycling requirement could be reduced, AlN would become more attractive, whereas for applications requiring a lower heat transfer efficiency, alumina would produce a larger design space.

B. Thermal Barrier Coating for a Gas Turbine Engine Combustor

Modern gas turbine engines commonly employ a ceramic thermal barrier coating on the hot side of a nickel superalloy combustor liner. The purpose of the coating is to act as an insulating layer and, hence, reduce the surface temperature of the metal so as to increase the component lifetime. This arrangement is shown schematically in Fig. 11.

The functional requirements of the substrate can be listed as follows.

1) The superalloy thickness must carry a certain stress level, due to the internal pressure loading. This defines a minimum thickness of the metal, e.g., 2.0 mm.

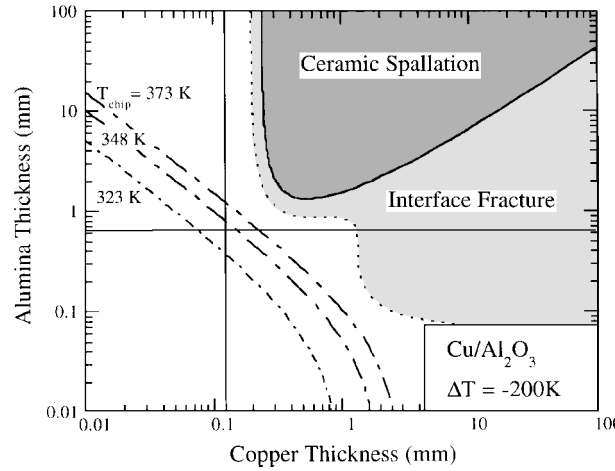

a) Cu/Al_2O_3

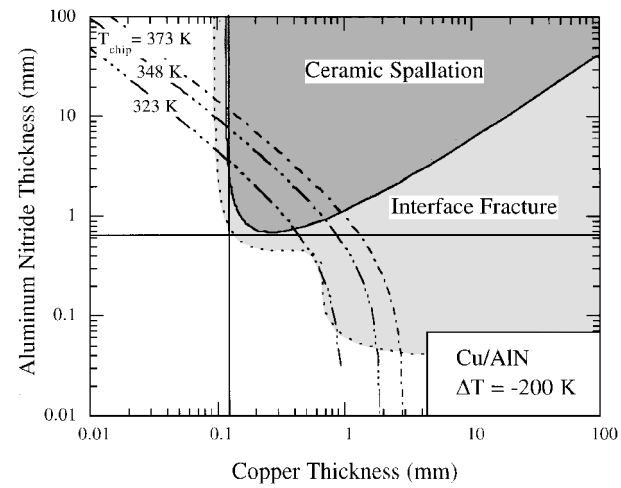

b) Cu/AlN

Fig. 10 Design diagrams for metal ceramic substrates for power electronics.

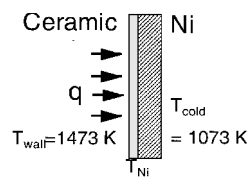

Fig. 11 Schematic of a thermal barrier coating on a nickel alloy combustor liner.

2) The peak metal temperature T_{Ni} must be maintained below a prescribed level, e.g., 1273 K. For illustrative purposes, it is assumed here that the material surface temperature T_{wall} is 1473 K and the outer wall of the combustor can be maintained at T_{cold} of 1073 K. Again, by one-dimensional heat flow, these quantities are related according to

$$T_{Ni} = \left[\frac{\kappa_2 t_1 T_{cold} + \kappa_1 t_2 T_{wall}}{\kappa_1 t_2 + \kappa_2 t_1}\right] \tag{13}$$

where κ_1 and κ_2 are the thermal conductivities of the two layers.

3) The combustor must survive thermal cycling of 273 K/1073 K.

4) The design must be achieved at minimum mass.

At the preliminary stage, it is insightful to compare the use of alumina as the ceramic coating against zirconia (ZrO_2). The relevant properties of the constituent materials are shown in Table 3. These properties are used to construct the design diagrams shown in Figs. 12a and 12b.

Inspection of Fig. 12 makes it very clear why zirconia is a widely used thermal barrier coating on nickel alloys whereas alumina is not. The larger thermal expansion mismatch, lower toughness, and relatively high thermal conductivity of alumina remove any possibility of achieving a reliable design. Whereas with zirconia, despite

Table 3 Properties of combustor liner constituents

	Ni	Al_2O_3	ZrO_2
Young's modulus E, GPa	200	370	200
CTE, $\alpha \times 10^{-6}$/K	17	8	9
Tensile strength σ_t, MPa	——	500	800
Toughness G_c, J/m^2	——	40	500
Conductivity κ, W/mK	50	21	3

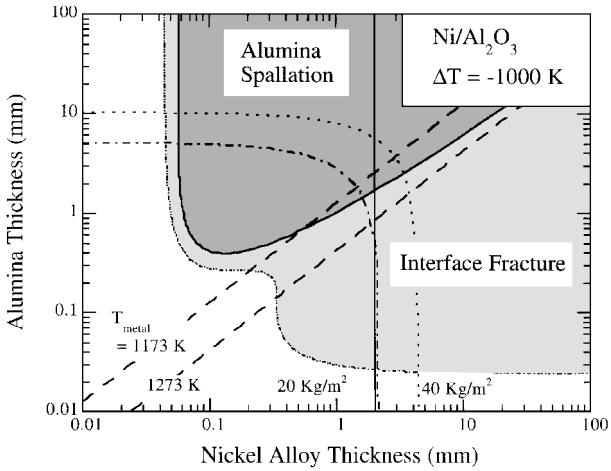

a) Al_2O_3

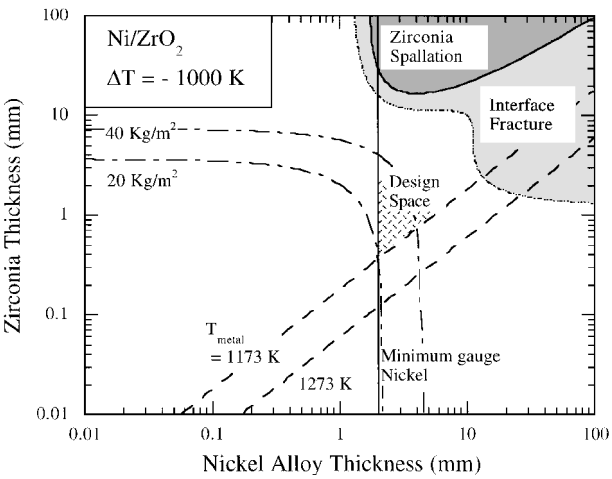

b) ZrO_2

Fig. 12 Design diagrams for thermal barrier coatings on Ni alloy combustor liners.

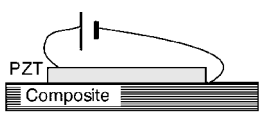

Fig. 13 Schematic of a PZT piezoceramic actuator on a graphite/epoxy panel.

its higher density, there is a clearly defined combination of layer thicknesses that can meet all of the functional requirements.

C. Active Composite Panel

The use of piezoceramic actuators for the dimensional and vibration control in various aerospace structures is gaining acceptance.[4] Typically, an actuator consists of a lead zirconium titanate (PZT) ceramic plate that is bonded to the surface of the structure to be controlled. This is shown schematically in Fig. 13.

For a space vehicle application the functional requirements might be stated as follows.

1) The composite panel has to carry inertial loads at launch, which effectively define a minimum thickness of the panel, e.g., 2 mm.

2) The ceramic strains under the electric field, a free activation strain of 1000 microstrain can be achieved. For the particular case,

Table 4 Properties of PZT actuator and composite laminate

	PZT	Graphite/epoxy
Young's modulus E, GPa	60	70
CTE, $\alpha \times 10^{-6}$/K	4	0
Tensile strength σ_t, MPa	50	500
Toughness G_c, J/m^2	25	200
Density ρ, Mg/m^3	7.4	2.0

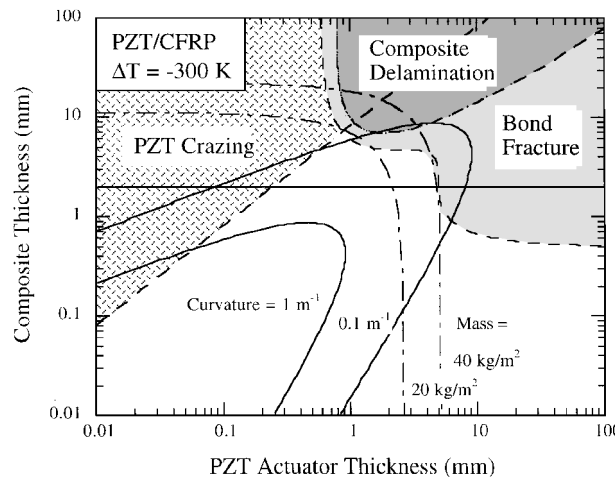

Fig. 14 Design diagram for a PZT actuator bonded to a laminated graphite/epoxy panel.

the aim is to control the curvature of the composite panel; this can be calculated using simple beam theory. A higher curvature for a given applied voltage indicates a higher activation authority.

3) The PZT/composite assembly must survive thermal cycling (123/423 K).

4) The design must be achieved at a minimum mass.

The relevant properties are given in Table 4. Figure 14 shows the calculated design map for such an active panel. The functional requirements can be readily met if a 1-mm-thick PZT actuator is used in combination with a 2-mm-thick composite panel. This achieves the highest possible actuation authority for the minimum mass per unit area while lying as far from the boundaries of the failure modes as is possible.

V. Discussion and Summary

The map formats presented in Secs. III and IV form a useful foundation for the discussion of design strategies, experimental results, and observations of failure. More complicated components can be approximated, for preliminary consideration as elastic bilayers, with one critical interface. Clearly, more sophisticated treatments are needed as more accurate analysis is required. For instance, hitherto no attempt has been made to account for the role of plate deformation modes, material nonlinearity, three-dimensional effects, edge effects, and the effect of nonisothermal conditions. These can be included, albeit at the expense of simplicity, by using numerical methods. Further work is needed to extend the methodology to multilayers and different loading regimes, as well as fatigue processes. Despite these limitations the analysis methodology presented here represents a good starting point for the design process. The use of steady-state fracture solutions assuming elastic–brittle material behavior gives solutions that are conservative lower bounds to the behavior that is observed experimentally.

We have endeavored to combine and extend existing mechanical analyses to help understand the cause and interaction of failure modes of an elastic bilayer under thermomechanical loading. The key insight is that for a pair of elastic materials there are four distinct failure modes that may operate: crazing of either layer, spalling, and interfacial fracture. The analyses are presented as failure mode maps. In combination with simple models for other aspects of the component's performance, multifunctional design diagrams can be

constructed. These diagrams are readily used for preliminary design, presentation of experimental data, and failure mode analysis. They are also useful educational tools to allow members of design teams with different disciplinary backgrounds to understand the tradeoffs involved in the overall design process.

References

[1]Tummala, R. R., and Rymaszewski, E. J., *Microelectronics Packaging Handbook*, Van Nostrand Reinhold, New York, 1989, Chap. 5.

[2]Cammarata, R. C., Chung, D. D. L., and Jono, M., "Mechanical Behavior of Materials and Structures in Microelectronics," *Materials Research Society Symposia Proceedings*, Vol. 226, edited by E. Suhir, Materials Research Society, Pittsburgh, PA, 1991, pp. 269–277.

[3]Dodds, W. J., and Bahr, D. W., "Combustion Systems Design," *Design of Modern Turbine Combustors*, edited by A. M. Mellor, Academic, New York, 1990, Chap. 4.

[4]Lazarus, K. B., and Crawley, E. F., "Multivariable High-Authority Control of Plate-like Active Structures," AIAA Paper 92-2529, April 1992.

[5]Vinson, J. R., Mall, S., and Leichti, K. M. (eds.),*Advances in Adhesively Bonded Joints*, Vol. 6, Materials Div., American Society of Mechanical Engineers, New York, 1988, pp. 1–111.

[6]Hutchinson, J. W., and Suo, Z., "Mixed Mode Cracking in Layered Materials," *Advances in Applied Mechanics*, Vol. 29, 1991, pp. 63–191.

[7]Hu, J. M., Pecht, M., and Dasgupta, A., "Design of Reliable Die Attach," *International Journal of Microcircuits and Electronic Packaging*, Vol. 16, No. 1, 1993, pp. 1–15.

[8]Drory, M. D., Thouless, M. D., and Evans, A. G., "On the Decohesion of Residually Stressed Thin Films," *Acta Metallurgica*, Vol. 36 , 1986, pp. 2019–2028.

[9]Spearing, S. M., Tenhover, M. A., Lukco, D. B., Viswanathan, L., and Hollen, D. K., "Models for the Thermomechanical Behavior of Metal/Ceramic Laminates," *Electronic Packaging Materials Science VII*, *Materials Research Society Symposia Proceedings*, Vol. 323, Materials Research Society, Pittsburgh, PA, 1994, pp. 125–130.

[10]Timoshenko, S., *Strength of Materials*, 2nd ed., Vol. 1, Van Nostrand, New York, 1940, pp. 217–219.

[11]Boley, B. A., and Weiner, J. H., *Theory of Thermal Stresses*, Krieger, Malabar, FL, 1985, pp. 429–431.

[12]Suo, Z., and Hutchinson, J. W., "Steady State Cracking in Brittle Substrates Beneath Adherent Films," *International Journal of Solids and Structures*, Vol. 25, No. 11, 1989, pp. 1337–1353.

[13]Dundurs, J. J., "Edge Bonded Dissimilar Orthogonal Elastic Wedges Under Normal and Shear Loading," *Journal of Applied Mechanics*, Vol. 36, Sept. 1969, pp. 650–652.

[14]Evans, A. G., and Hutchinson, J. W., "Thermomechanical Integrity of Thin Films and Multilayers," *Acta Metallurgica et Materialia*, Vol. 43, No. 7, 1995, pp. 2507–2530.

[15]Nix, W. D., "Residual Stresses and Fracture of Thin Films," *Metallurgical Transactions A*, Vol. 20A, No. 11, 1989, pp. 2217–2225.

[16]Reimanis, I. E., Dalgleish, B. J., and Evans, A. G., "The Fracture Resistance of a Model Metal/Ceramic Interface," *Acta Metallurgica*, Vol. 39, No. 12, 1991, pp. 3133–3141.

[17]Dalgleish, B. J., Lu, M. C., and Evans, A. G., "The Strength of Ceramics Bonded with Metals," *Acta Metallurgica*, Vol. 36, No. 8, 1988, pp. 2029–2035.

[18]Bagchi, A., Lucas, G. E., Suo, Z., and Evans, A. G., "A New Procedure for Measuring the Decohesion Energy For Ductile Films on Substrates," *Journal of Materials Research*, Vol. 9, No. 7, 1994, pp. 1734–1741.

[19]Beyerle, D. S., Spearing, S. M., Zok, F. W., and Evans, A. G., "Damage and Failure in Unidirectional Ceramic-Matrix Composites," *Journal of the American Ceramic Society*, Vol. 75, No. 10, 1992, pp. 2719–2725.

[20]Spearing, S. M., and Evans, A. G., "The Role of Bridging Fibers in the Delamination of Brittle Matrix Composites," *Acta Metallurgica et Materialia*, Vol. 40, No. 9, 1992, pp. 2191–2199.

[21]Yoshino, Y., Ohtsu, H., and Shibata, T., "Thermally Induced Failure of Copper Bonded Alumina Substrates for Electronic Packaging," *Journal of the American Ceramic Society*, Vol. 75, No. 12, 1992, pp. 3353–3357.

A. M. Waas
Associate Editor